Mechanical properties and microstructural characterisation including high-temperature performance of Al-Mn-Cr-Zr-based alloys tailored for

Citation for the original published paper (version of record):
Mehta, B., Bengtsson, S., Riabov, D. et al (2024). Mechanical properties and microstructural characterisation including high-temperature
performance of Al-Mn-Cr-Zr-based alloys tailored for additive manufacturing. Materials and Design, 244. http://dx.doi.org/10.1016/j.matdes.2024.113160

(article starts on next page)

Materials & Design 244 (2024) 113160

Contents lists available at ScienceDirect

Materials & Design

journal homepage: www.elsevier.com/locate/matdes

Mechanical properties and microstructural characterisation including high-temperature performance of Al-Mn-Cr-Zr-based alloys tailored for additive manufacturing

Bharat Mehta [a,b,*], Sven Bengtsson [a,c], Dmitri Riabov [a,c], Elanghovan Natesan [a], Karin Frisk [a], Johan Ahlström [a], Lars Nyborg [a]

[a] Department of Industrial and Materials Science, Chalmers University of Technology, Rännvägen 2A, Göteborg 412 96, Sweden
[b] Department of Materials Science and Engineering, KTH Royal Institute of Technology, Brinellvägen 23, Stockholm 100 44, Sweden
[c] Höganäs AB, Bruksgatan 35, Höganäs 263 39 Sweden

ARTICLE INFO

Keywords:
Additive manufacturing
Powder bed fusion-laser beam
Aluminium alloys
Precipitation hardening
Mechanical properties
High-temperature materials

ABSTRACT

Powder bed fusion-laser beam (PBF-LB), an additive manufacturing process, takes advantage of rapid cooling rates (10^3-10^6 K/s) to enable novel aluminium alloys. This study reports the mechanical properties of one such alloy system (Al-Mn-Cr-Zr based). The alloys based on this system are designed to be precipitation hardenable with high service temperatures. To elucidate the precipitation hardening, three alloy variants were studied involving different heat-treated conditions. Uniaxial tensile testing at room temperature revealed yield strengths between 250–500 MPa with elongation to fracture of 5–25 % with high repeatability. To demonstrate high-temperature resistance, two alloy variants in peak hardened condition were tested at temperatures of up to 573 K. Yield strength up to 170 MPa at 573 K was observed. These properties in combination demonstrate highly competitive Al-alloys for high-temperature applications.

1. Introduction

Metal additive manufacturing (AM) as a preferred technology is becoming commonplace for small to medium-scale production [1,2]. The benefits of this technology are related to both improved product design and novel material concepts. Particularly for the powder bed fusion-laser beam (PBF-LB) process, which is the most used metal AM process [3], the design benefits are evident. The PBF-LB process opens the possibility to design complex internal structures and lattice structures that are difficult to manufacture with other techniques [4,5,6]. Novel microstructures are enabled via PBF-LB, as shown by several authors [7,8,9]. To take full advantage of the materials design capabilities of AM, it is of interest to have access to light alloys with high specific strength. Thus, the development of high-strength aluminium (Al) alloys for the PBF-LB process has consequently gained attention, see for example [6,10].

Al-alloys for PBF-LB initially found their way into commercial application with the AlSi10Mg and AlSi7Mg alloys developed based on their cast alloy counterparts [11,12]. Utilising the processing conditions in PBF-LB combined with eutectic solidification produced finer microstructures compared to cast counterparts [13]. This provided a blend of good mechanical properties and easy manufacturability when produced using PBF-LB. However, these alloys fall short of conventional high-strength Al-alloys (strengths > 450 MPa), which gain their strength from finely dispersed precipitates [10,14]. Over time, researchers, therefore, developed and commercialised high-strength Al-alloys such as Scalmalloy® [15,16], A20X® [17,18] or Al2139 [19] whereby the PBF-LB process provide a basis to add novel alloying elements and reach competitive strength levels. Similar to conventional high-strength Al-alloys, precipitation hardening was the biggest contributor to strength. Some strength is also derived from grain refinement, solid solution strengthening and dislocation strengthening. Nevertheless, these alloys were based on a known Al-alloy grade and therefore did not consider the benefit of extended solubility (specifically of transition series metals) inherent to the PBF-LB process [20,21]. Recently, some authors [9,21,22,23,24,25] have showcased that CALPHAD coupled tools may be utilised to enable Al-alloys tailored for PBF-LB process exploring new elements outside the known Al-grades. The alloys developed were targeted towards high strength, or in some cases secondary properties such as high-temperature strength. The reason why high-temperature

* Corresponding author.
E-mail address: bmehta@kth.se (B. Mehta).

https://doi.org/10.1016/j.matdes.2024.113160
Received 6 March 2024; Received in revised form 31 May 2024; Accepted 9 July 2024
Available online 14 July 2024

strength is lucrative is that, as per [26,27], improving the operating temperature of Al-alloys from 473 K to 573 K could be extremely beneficial for wider adoption. This could challenge the use of Ti-alloys or Fe-alloys in some applications. Conventional high-strength Al-alloys possess strengths < 80 MPa at 573 K [28]. Some authors have recently presented novel Al-alloys for PBF-LB such as Al-Ce-Mn [29] and Al-Fe-Cr [30] which show strengths ~ 150–200 MPa at temperatures > 573 K. However, there is then a compromise on the room temperature strengths of these alloys as compared to the high-strength Al-alloys.

The Al-Mn-Cr-Zr based alloy system has been presented by the authors before [21,31,32]. This alloy system is characterised by good printability combined with high supersaturation of elements such as Mn, Cr and Zr. This provides good as-printed hardness (between 85–130 HV) and a strong hardening response (~40 HV increase) on direct ageing heat treatments. The alloy system has been designed for high-temperature stability [21,33]. One part of this stability has been illustrated before with long-term experiments at 623 K for ~ 1000 h showing only a 12 % drop (17 HV) from initial peak hardness [33]. In this study, the assessment of mechanical properties is conducted to cover three alloy variants within this alloy system. We reported room temperature properties after different heat treatments for several samples along two different building directions. Two of the alloy variants in peak hardened condition are also tested at high temperatures (up to 573 K) to showcase high-temperature properties. The resulting mechanical properties are then coupled with the assessment of strengthening mechanisms using CALPHAD tools, advanced materials characterization involving transmission electron microscopy (TEM) and fractography. The studies intend to show that the Al-Mn-Cr-Zr based alloys combine excellent room temperature and high-temperature properties to create a novel class of high-temperature Al-alloys.

2. Materials and methods

2.1. Materials

Spherical powder of three alloy compositions was fabricated by nitrogen gas atomization and provided by Höganäs AB, Sweden with powder size distribution of 20–53 μm diameter. The specifications of powder size distribution have been detailed elsewhere [21]. The chemical composition of the three variants, determined via ICP-OES analysis at Höganäs AB, Sweden are summarised in Table 1; data taken from [21,32].

2.2. Modelling

For thermodynamic modelling, Thermo-Calc 2022a software with TCAL8 and MOBAL6 databases was used. The PRISMA precipitation toolbox [34] was used for depicting precipitation kinetics, involving calculating the mean radius and volume fraction of precipitates formed during isothermal heat treatments.

2.3. PBF-LB processing and post-processing treatments

All three alloy variants were manufactured using an EOS M290 machine with a 100 μm spot size and 370 W nominal power Yb-fibre laser. Samples were processed in an inert argon atmosphere with a standard oxygen level set and controlled at a maximum of 0.1 %. The samples were printed at 370 W power, 1300 mm/s laser scanning speed, 0.13 mm hatch distance and 0.03 mm layer thickness to produce fully dense samples (>99.8 % relative bulk density). These parameters were selected based on previous work where process optimisation was done utilising a design of experiments approach [32]. Scan rotation of 67° between each layer of material deposition was applied. The heat treatments for all the samples were conducted in a radiation-controlled furnace with a temperature control of ± 2 K. The samples were heated to optimum heat treatment temperature (623/ 648 K) at 10 K/min. The optimum heat treatments are based on previous work [32]. After heat treatment, the samples were air-cooled.

Table 1
Summary of alloy chemistries (weight%/atomic%). Fe and Si are considered impurities.

Alloy studied	Al	Mn	Cr	Zr	Mg	Fe	Si
Alloy C	Rem.	5.0/ 2.53	0.8/ 0.43	0.6/ 0.18	–	0.17/ 0.08	0.24/ 0.24
Alloy D	Rem.	4.7/ 2.39	0.8/ 0.43	1.2/ 0.37	–	0.13/ 0.06	0.21/ 0.21
Alloy F	Rem.	4.8/ 2.41	0.9/ 0.48	1.1/ 0.33	1.2/ 1.36	0.19/ 0.09	0.20/ 0.20

2.4. Microstructural characterization

The samples for scanning electron microscopy (SEM) were prepared from 10 mm side cubic samples printed in the same build job. The samples were cut followed by grinding up to 4000 grit silica foil and polished up to 1 μm diamond-based polish for preparing such alloys as mentioned elsewhere [31]. After polishing, a final step using OP-S silica suspension from Struers was applied. All the samples were prepared using a Struers TegraPol 31 machine. Fresh fracture surfaces from tensile samples were cleaned with ethanol before characterisation to remove possible contaminations. Light optical microscopy was conducted using a Zeiss Axioscope 7 microscope for general characterization. Stereo optical microscopy was conducted on a Zeiss stereo discovery.V20 stereo optical microscope. High magnification microstructural characterisation was done with a Zeiss Gemini 450 SEM equipped with a field emission gun source. The SEM is fitted with ULTIM MAX Energy Dispersive X-ray Spectroscopy (EDS) detector from Oxford Instruments, which enables elemental mapping of microstructure at sub-micron resolutions due to low beam voltage. The samples for transmission electron microscopy (TEM) were prepared by thinning down slices (1 mm) of samples along the Z direction to 0.1–0.12 mm thin foils. These thin foils were then punched into 3 mm diameter disks followed by twin-jet electropolishing using Struers Tenupol 5. Struers A2 electrolyte was used at a temperature of 243 K at a polishing voltage of 15 V. For TEM a Tecnai T20 using an accelerating voltage of 200 kV was used and images were taken in bright-field.

2.5. Mechanical testing

All the PBF-LB processed samples for testing were cut from the build plate with a cold band saw. The samples for room temperature (RT)

Table 2
Summary of samples for room temperature and high-temperature tensile testing.

Room temperature (RT) tensile testing		
Alloy	Direction of testing	Heat treatment
Alloy C	Z XY	As printed, 623 K 24 h (HT1), 648 K 14 h (HT2)
Alloy D	Z XY	As printed, 623 K 24 h (HT1), 648 K 4 h (HT2)
Alloy F	Z XY	As printed, 623 K 24 h (HT1), 648 K 8 h (HT2)

High-temperature tensile testing			
Alloy	Direction of testing	Heat treatment	Temperature of testing
Alloy C	Z XY	648 K 14 h	RT (298 K), 423 K, 473 K, 523 K, 573 K
Alloy F	Z XY	648 K 8 h	RT (298 K), 423 K, 473 K, 523 K, 573 K

tensile testing were heat treated as per specifications summarised in Table 2 and then machined to the final shape (see Fig. 1) from the original cylindrical shape. Seven samples for each condition and build direction (Z and XY) were tested. All the samples were tested at Höganäs AB, Sweden using a Zwick Z100 tensile testing machine with a 100 kN load cell. The extensometer used had a gauge length of 25 mm. RT tensile tests were conducted in displacement control till yield at 0.45 mm/min, following which they were tested at 10 mm/min after yield.

The samples for high-temperature tensile testing were heat treated as summarised in Table 2 and then machined to the final shape (see Fig. 1). Three samples for each condition and build direction (Z and XY) were tested. Along the XY direction, it was judged sufficient to test one sample at 423 K, 473 K, and 523 K. Testing was conducted at Chalmers University of Technology on an Instron 8501 servo-hydraulic testing machine equipped with a fast electronic control system and 1 kHz data logging system. Two hours of soaking at a set temperature was done before starting tests to account for thermal expansion during temperature stabilization in the test rig. Testing was conducted with a strain rate of 0.01 % s^{-1}, where the strain was measured with an extensometer. In one case (alloy C, Z direction), a strain rate of 1 % s^{-1} was applied at 298 K and 573 K to characterize strain rate sensitivity.

3. Results

3.1. Room temperature uniaxial tensile testing

Fig. 2 shows the summary of uniaxial tensile properties in the form of a scatter curve with solid black lines representing the mean values. A low scatter is observed for the presented data except for a few stray measurements for alloy D. Fig. 3 illustrates engineering stress (MPa) v/s elongation to failure (%) curves for one representative sample for all 18 conditions tested. In as-printed (AP) condition the alloys showed relatively high elongation to failure (>15 %) with yield strength (YS) between 250–400 MPa. Alloy C showed isotropic YS along both directions whereas alloys D and F had about a 30 MPa difference in yield strength when comparing the two directions of loading. Alloy D showed a relatively low strain hardening ratio in the AP condition which is visible in Fig. 2d). Instability in the plastic zone during tensile testing, also called the "Portevin-Le-Chatelier" (PLC) effect as reported previously [36,37] for Mg-containing Al-alloys was observed in alloy F as-printed condition, see Fig. 3 e)-f). Post heat treatments, all the alloys gained significant strength with a reduction in ductility as expected from precipitation-hardened Al-alloys [14,18,19]. Alloys C and D showed similar tensile responses for most conditions with YS at about 350 MPa. Alloy F showed high YS reaching 500 MPa for all the conditions, although lower ductility (3–7 %) was observed. The PLC effect was not observed in heat-treated conditions for alloy F.

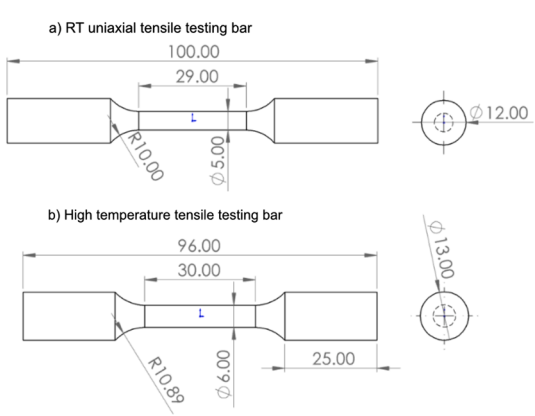

Fig. 1. Two-dimensional sketch for final dimensions of a) uniaxial tensile testing bar and b) high-temperature tensile testing bar. Radius (R) represents the minimum value. All dimensions in mm. Machined samples follow specifications from ASTM E8 standard [35].

Fractography was conducted on several samples after tensile testing. A summary of fractography on selected samples is shown in Fig. 4. In general, all the alloys showed the formation of micro dimples. Alloy C and F when tested along the Z direction (HT2 condition) showed distinct fractures resembling melt pool tracks, which were rich in melt pool boundary precipitates. Along XY direction (Fig. 4c)), it is seen that intergranular fracture might have taken place with fracture surfaces along grain boundaries being more visible. Grain boundaries were confirmed via apparent size of features and confirming the chemical composition of precipitates similar to grain boundary precipitates formed upon heat treatments.

3.2. High-temperature uniaxial tensile testing

High-temperature tensile testing was conducted in peak hardened conditions at 423–573 K (see Table 2). As this experiment was performed with a different test setup and in a strain-controlled regime, another set of samples was tested at RT (298 K) for consistency and fair comparison to the high-temperature tests. Fig. 5 summarises the results in the form of a scatter curve starting from RT up to 573 K. The error bars represent three standard deviations for better visualisation of data as the scatter was low. One representative sample each from alloy C and alloy F at all the temperatures of testing is shown in Fig. 6. The drop in UTS of 400 MPa at RT to ~ 180 MPa (45 % of RT strength) at 573 K was observed for alloy C. The elongation to failure reduced drastically along the XY direction to ~ 2 % at 573 K whereas this reduction was less severe along the Z direction (~6% at 573 K). For alloy F, UTS of 550 MPa at RT reduces to ~ 125 MPa (23 % of RT strength) at 573 K. Unlike alloy C, the elongation to failure increased for alloy F along XY direction and > 15 % was observed for 573 K. Along Z direction, this trend was not observed, a rather similar trend to alloy C with reduced ductility with ~ 5 % elongation at 573 K.

Fractography conducted on some of the high-temperature samples is shown in Fig. 7. Along the Z direction, a similar trend of fracture along melt pool tracks (see Fig. 4 b),d)) was observed for both alloys. Fractures also progressed perpendicular to melt pool tracks, which were seen to be rich in precipitates. The orientation and size of features suggest that these resemble the distance between solidification boundaries which are rich in needle-/plate- shaped nanoprecipitates. Along XY direction, intergranular fracture with fracture surfaces decorated by solidification boundary and grain boundary precipitates (similar to Z direction). In this case, however, the melt pool boundary did not seem to connect the fracture surfaces (see Fig. 7b)).

3.3. Strain-rate sensitivity tensile testing

Strain-rate sensitivity tests comparing room temperature and 573 K for alloy C (peak aged, Z direction) were conducted by increasing strain rate (0.01 % s^{-1} to 1 % s^{-1}). A summary of the tests is provided in Fig. 8. Work hardening is enhanced in both cases (RT and 573 K) thereby increasing the UTS by ~ 35–40 MPa. A similar observation could be made comparing tensile tests in Fig. 3 and Fig. 6 where RT samples were tested in displacement control at a high-speed post-yield point (Fig. 3) and constant strain rate for the entire test (Fig. 6).

3.4. Microstructure of as-printed and peak-aged samples

Fig. 9 shows the summary of microstructures for all three alloys in as-printed condition as viewed on cross-section along the Z direction of printing. The insets illustrate the centre of the melt pools (green) and the melt pool boundary (blue) respectively. In as-printed conditions, there is saturation beyond equilibrium for alloys C (~1% area) with nano-precipitates < 100 nm locally segregated along solidification boundaries and relatively larger primary precipitates (<500 nm) formed along melt

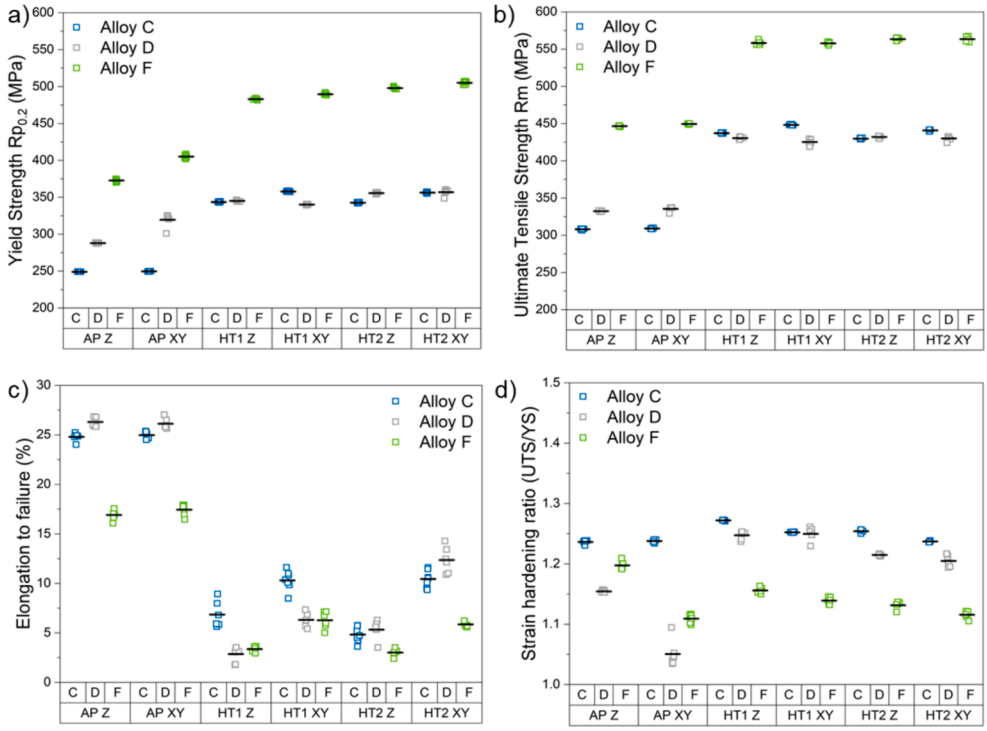

Fig. 2. Summary of mechanical properties for alloy C, D, F along Z and XY directions in as-printed (AP) and two heat-treated (HT1, HT2) conditions a) Yield strength (MPa) b) Ultimate tensile strength (MPa) c) Elongation to failure (%) and d) Strain hardening ratio. Some values for alloy C were also reported previously in [38].

pool boundaries respectively. A slight increase in primary precipitation for alloy D (~3% area) is observed. For alloy F, a higher Mg content promotes primary precipitation by affecting solidification conditions leading to primary precipitation of ~ 8 % for as-printed conditions. Please refer to our previous work for detailed discussion [21,32,39].

Microstructure for peak aged condition was characterised for samples in HT2 condition (648 K) along the Z direction of printing. Fig. 10 shows an overview of the microstructure. In our previous works [31,40], it has been shown that the secondary Mn-containing precipitates grow differently at the centre of the melt pool than at melt pool boundaries. Larger precipitates at grain boundaries are observed and finer needle-/plate-shaped Mn-rich precipitates are seen inside the grains (see Fig. 10). The two high magnification insets (purple) for alloys C and F both show similar morphology of these finer precipitates. The precipitates in alloy C are slightly larger and appear denser in number than alloy D and alloy F which may be due to longer heat treatment times for alloy C (14 h) as compared to alloy D (4 h) and alloy F (8 h). Precipitate-free zones (PFZs) were seen in all alloys, with a clear depiction in alloy F. These PFZs were less pronounced in alloy C. The second category of precipitates namely at melt pool boundaries do not change much during heat treatments (see insets in blue). For alloys D and F, which contain refined grains concentrated at melt pool boundaries, larger grain boundary precipitates are also observed.

Furthermore, TEM characterization for two different heat treatment conditions for alloy C was conducted namely 14 h and 24 h at 648 K to characterize the Al_3Zr nanoprecipitates. The aim was to identify the average size and area fraction of these nanoprecipitates. TEM was needed as these precipitates are too fine to be characterized by SEM. The TEM micrographs of alloy C in peak hardened condition (ageing for 14 h at 648 K) are presented in Fig. 11. The Al-Zr-containing precipitates were not visible at lower magnifications in bright fields, nor were any additional diffraction spots visible in the selective area diffraction pattern. After tilting to the [001] zone axis and performing high-resolution TEM the precipitates started being visible as dark circular features. Fast-Fourier transforms on areas with circular features revealed additional reflections, supporting that these were precipitates. Based on literature evidence [41,42] and the size of the precipitates, we believe that these precipitates are $L1_2$-type Al_3Zr nanoprecipitates. The super-reflections from the Fast-Fourier transform seem to support this. By measuring about 50 precipitates in three randomly selected areas, the mean radius (nm) and area fraction are estimated in Fig. 11 c)-d) with error bars representing one standard deviation. Area fraction was assumed to be similar to the volume fraction of precipitates in the whole lamella.

The calculations were then compared to PRISMA calculations conducted using Thermo-Calc software [34] for alloy C (disregarding Fe, Si) [34]. All the calculations were done for 648 K and a time of $2*10^5$ s (~55 h). A simplified growth rate model with molar volumes entered from a crystallographic database [43]. The grain size for the Aluminium matrix was assumed to be 20 μm with an aspect ratio set to 2 (based on data from our previous study [33]). The pre-mobility factor was adjusted to 10, to better mimic the conditions for the PBF-LB process. The mean radius values predicted with these assumptions were seen to be quite similar to the experimentally assessed values employing TEM experiments. The experimentally assessed volume fraction from TEM studies was, however, much higher compared to the theoretically predicted value of 0.007; one possible reason being the challenge with sample preparation, as discussed later.

4. Discussion

In this study, Al-Mn-Cr-Zr based alloys tailored for additive manufacturing are shown to produce mechanical properties competing with the state-of-art Al-alloys. To understand the underlying mechanism of strengthening in these alloys, it is important to understand how the microstructure develops during PBF-LB and how it further changes during heat treatments. Below, the generic outcome of the results in this study is analysed and reviewed in three parts, starting with the microstructure development during the PBF-LB process and post-processing heat treatments. This is followed by the effect of changing

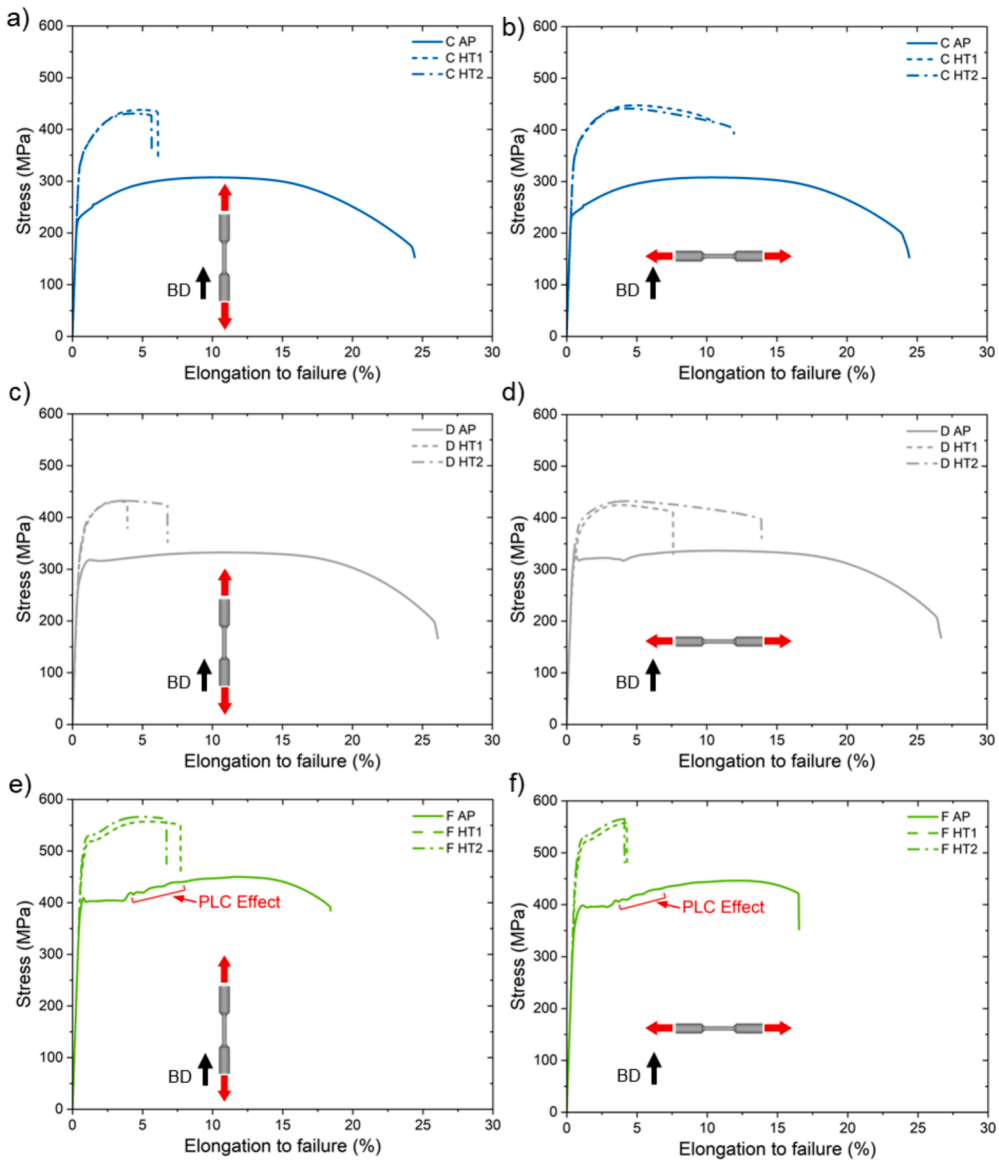

Fig. 3. One representative tensile curve for alloy C, D, and F printed along Z direction (a), c) and e)) and along XY directions (b), d) and f)) respectively. Three testing conditions namely as-printed (AP) and two heat-treated (HT1, HT2) conditions are shown. An illustration with building direction (BD) with a black arrow and tensile testing direction (red arrow) is shown in each graph for simplicity. (For interpretation of the references to colour in this figure legend, the reader is referred to the web version of this article.)

microstructure on the strengthening of the alloys at room temperature and high-temperature tensile performance combined with an analysis of the loss of ductility.

4.1. Microstructure development

Fig. 12 shows a simple explanation for microstructural development during the PBF-LB process for two extreme alloy variants namely alloy C and alloy F. Solidification in Alloy C leads to long columnar Al-grains along building direction, typical for many PBF-LB materials [44,45]. These grains can span across several layers of material deposition. This is supported by high cooling rates inherent to the PBF-LB process, which enables higher supersaturation of solutes during processing (shown previously in Fig. 9). However, locally within a melt pool there exists differences in thermal gradients (G) and growth rate (R) which causes a difference in microstructure within the deposited layer on a micrometre (μm) length scale, see Fig. 9. This effect is limited in alloy C to the formation of small melt pool boundary precipitates. In the case of alloy D (high-Zr) and alloy F (high-Zr and Mg-containing), this difference in G and R has a larger effect on the starting microstructure. One reason is that high-Zr level causes primary Al_3Zr formation in the melt at regions with low R (melt pool boundaries). As R increases towards the centre of melt pools, an increasing cooling rate causes solute trapping thus enabling higher solubility of Zr which prevents the formation of the primary precipitates [46]. The Al_3Zr precipitates formed at melt pool boundaries promote heterogeneous nucleation of Al-grains, thus effectively restricting grain growth between layers [42]. Additionally, we believe that Mg addition to this alloy [32] lowers the temperature of the last melt due to increased segregation thus promoting primary precipitation (as compared to alloy C and alloy D). This will lead to the formation of precipitates such as Mn-rich (Al_6Mn, $Al_{12}Mn$) or other low melting precipitates (alpha-AlMnSi or Mg_2Si) more evident in alloy F.

Upon heat treatment at 648 K, the microstructure develops as shown in Fig. 10. The changes to starting conditions for alloys with and without grain refinement affect the precipitate development during heat treatments. After heat treatments, the grain sizes are seen to be similar thus

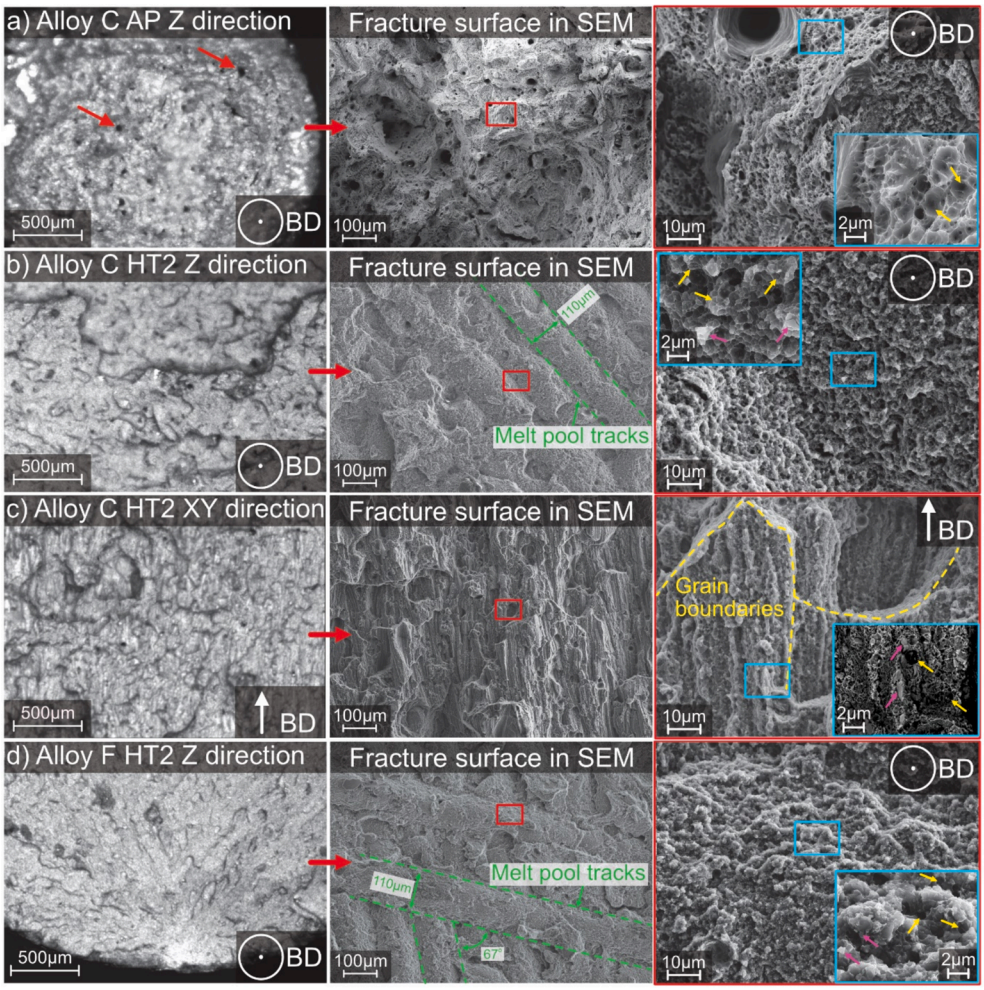

Fig. 4. Fractography summary for room temperature tensile samples a) Alloy C as-printed (AP) condition along Z direction b) Alloy C peak aged (HT2) along Z direction c) Alloy C peak aged (HT2) along XY direction and d) Alloy F peak aged (HT2) along Z direction. Higher magnification images in SEM reveal microstructural features such as melt pool tracks (green) and grain boundaries (yellow). Inset images (blue) show dimples (yellow arrows) and some precipitates (pink arrows) along fracture surfaces. (For interpretation of the references to colour in this figure legend, the reader is referred to the web version of this article.)

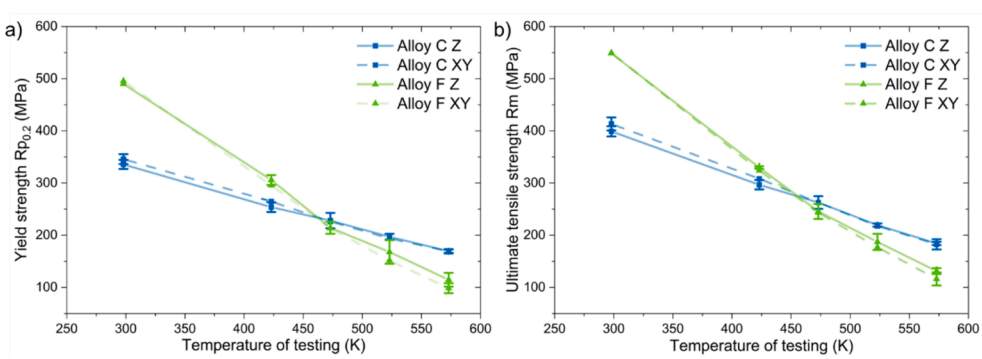

Fig. 5. Summary of high-temperature tensile result (starting from RT) for alloy C and F along Z and XY directions in peak aged (HT2) conditions. a) Yield strength (MPa) b) Ultimate tensile strength (MPa). Error bars representing three standard deviations are shown in tests where three samples were tested.

suggesting no significant recrystallisation has taken place. On a µm length scale, as was postulated by us before [21,31], three distinct precipitate regions are relevant namely the grain boundary region, inside the grains and melt pool boundaries. Preferential growth of precipitates at grain boundaries rich in Mn (tentatively containing Cr) was observed [31]. It was later confirmed during in-situ experiments that Cr-rich and Mn-rich phases co-precipitate at these locations during heat treatments which has not been reported before [40]. Inside the Al-grains, fine needle- /plate-shaped precipitates rich in Mn are observed that grow along solidification boundaries. Their small size (<200 nm) suggests that they could be providing strength to the matrix via Orowan looping. Their characterisation is currently ongoing and will be part of future work. As seen in Fig. 10e) precipitate free zones (PFZs) started to become evident at high resolution which is often a cause for ductility loss in precipitation-hardened Al-alloys [47], as discussed later. The third region namely melt pool boundaries contains precipitates that are

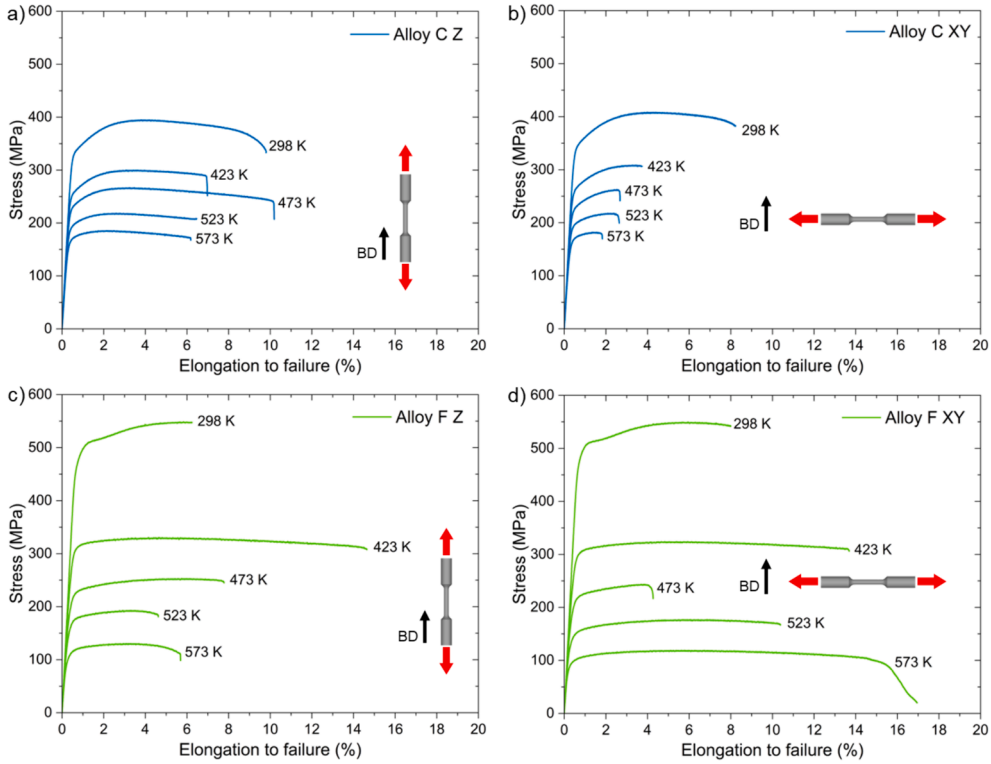

Fig. 6. One representative high-temperature tensile curve (starting at RT) for a)-b) alloy C and c)-d) alloy F printed along the Z direction and XY direction respectively. All the samples are in their respective peak-aged condition. An illustration with building direction (BD) with a black arrow and tensile testing direction (red arrow) is shown in each graph for simplicity. (For interpretation of the references to colour in this figure legend, the reader is referred to the web version of this article.)

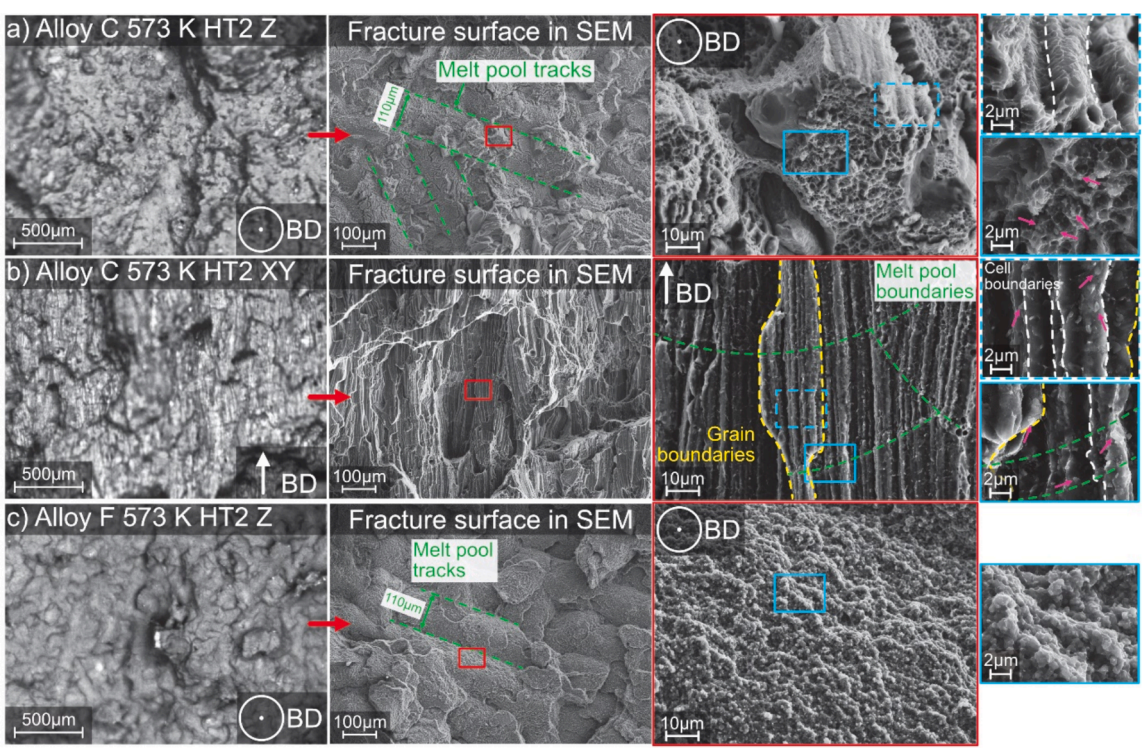

Fig. 7. Fractography summary for high-temperature tensile samples tested at 573 K a) Alloy C HT2 condition along Z direction b) Alloy C HT2 condition along XY direction and c) Alloy F in HT2 condition along Z direction. Higher magnification images in SEM reveal more information. Microstructural features such as melt pool tracks or melt pool boundaries (green), grain boundaries (yellow) and cell boundaries (white) are shown. Inset images (blue) show the decoration of precipitates (pink arrows) along fracture surfaces. (For interpretation of the references to colour in this figure legend, the reader is referred to the web version of this article.)

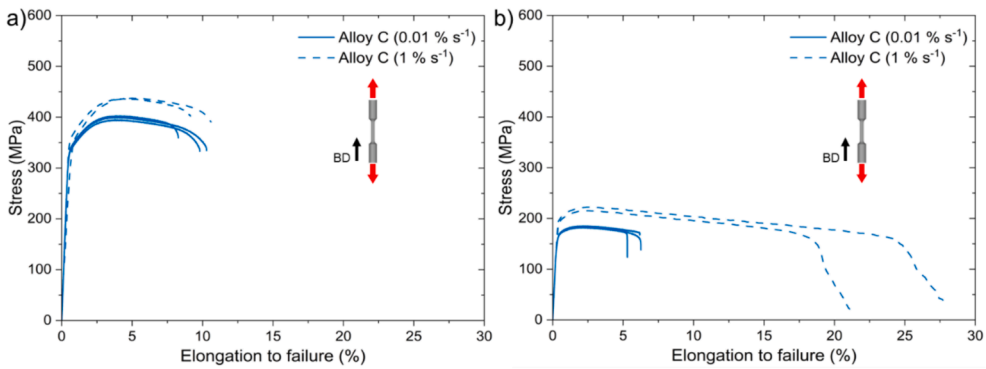

Fig. 8. Strain rate sensitivity for alloy C along Z direction. Two strain rates were shown (0.01 % s^{-1} and 1 % s^{-1} tested with the former reported in Fig. 6 as well). a) Room temperature (298 K) samples and b) High temperature (573 K) samples. All the samples are in their respective peak-aged condition. An illustration with building direction (BD) with a black arrow and tensile testing direction (red arrow) is shown in each graph for simplicity. (For interpretation of the references to colour in this figure legend, the reader is referred to the web version of this article.)

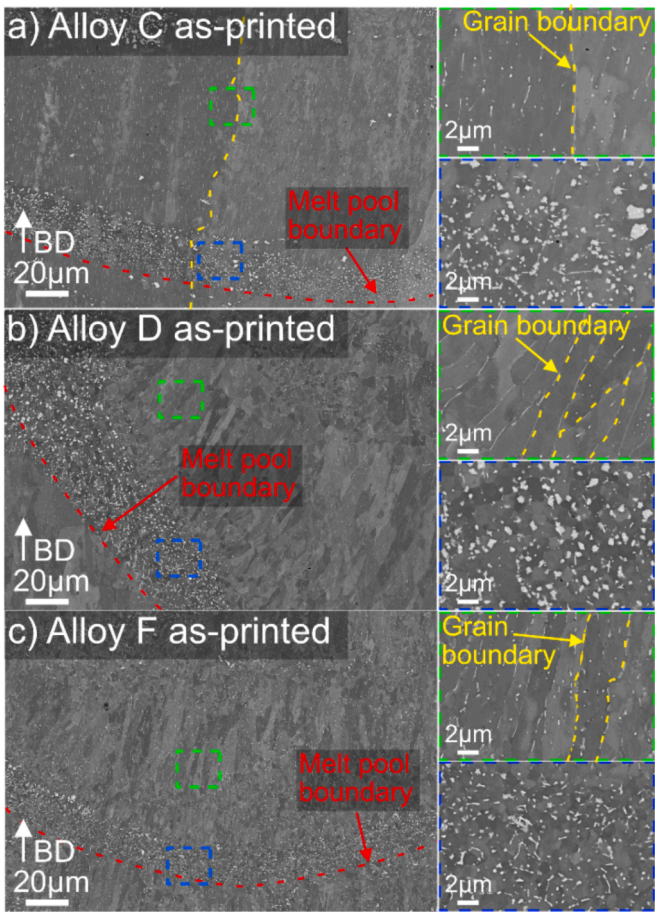

Fig. 9. As-printed microstructure of a) Alloy C b) Alloy D and c) Alloy F along building direction (BD). Melt pool boundaries and grain boundaries are marked with red and yellow dotted lines respectively. The insets for each micrograph represent high-resolution images of the interior of the melt pool (green) and melt pool boundary (blue) region. (For interpretation of the references to colour in this figure legend, the reader is referred to the web version of this article.)

largely unaffected during heat treatments and do not change in shape or size. During in-situ experiments [40] it was seen that these precipitates contain Mn and Cr, and their concentration stays stable during heat treatments. It can be added, however, that the fine needle- / plate-shaped precipitates are not observed in these regions which could be a sign of Al-solid solution being depleted in Mn, Cr in these regions. Finally, on a nanometre scale, there is the development of Zr-rich nanoprecipitates as confirmed in Fig. 11, which should provide the primary strength increase to these alloys as discussed in the following sections.

4.2. Resulting mechanical properties

As introduced before, the total strength in Al-alloys is considered as a sum of five effects namely the inherent strength of pure-Al, solid solution effect, grain boundary effect, dislocation strengthening and precipitation hardening. Table 3 summarises the actual yield strength of two of the alloys namely alloy C and alloy F in AP and HT conditions. The values are taken from room temperature tensile tests and averaged along Z and XY directions. It was then compared with a sum of contributions (except the solid solution effect) to describe the remaining strength as possible solid solution strength. A detailed description calculating each of the strengthening effects is provided in the supplementary section.

In as-printed conditions, both alloy C and alloy F have relatively low yield strength since a large part of the strength is derived from the solid solution effect. Since alloy F contains dissolved Mg, this effect is larger [32]. Additionally, the precipitation hardening and grain size effect is high for alloy F due to grain refinement, as shown previously in Fig. 9 and Fig. 12. This provides an overall higher as-printed strength (+140 MPa) as compared to Alloy C. In the peak aged conditions, the alloying elements in solid solution (Mn, Cr, Zr) precipitate into fine nanometric precipitates and the strength shifts to precipitation hardening. Our calculations show that precipitation hardening of 242 MPa and 374 MPa are possible in alloy C and alloy F respectively, which is the main reason for the large difference in strength of these alloys. There are two reasons for this increased precipitation hardening for alloy F. The first is that due to the solute trapping effect [46] and the higher Zr content (1.1 wt%), the centre of melt pools in alloy F will have a higher solubility of Zr which means a higher amount of Al_3Zr nanoprecipitates are possible. As per our estimate, this would also mean ~ 55 MPa higher strength (see supplementary material for calculations). Additionally, the refined grains in alloy F together with the presence of Mg [32,48] will modify the precipitation kinetics which means that the volume fraction needed for optimum precipitation response is reached sooner (8 h instead of 24 h) and an additional 100 MPa strength is possible. However, the feature analysis method used for studying precipitate size and amount relies on backscattered electrons to identify the contrast between Mn-precipitates and Al-matrix. At the same time, different Al-grain orientations become visible thus introducing difficulties in making the analysis, especially with alloy F containing refined grains. This means that the precipitation hardening for Mn-precipitates for alloy F may be overestimated and a relatively higher strength contribution could come from the solid solution effect (currently 23 MPa, see Table 3).

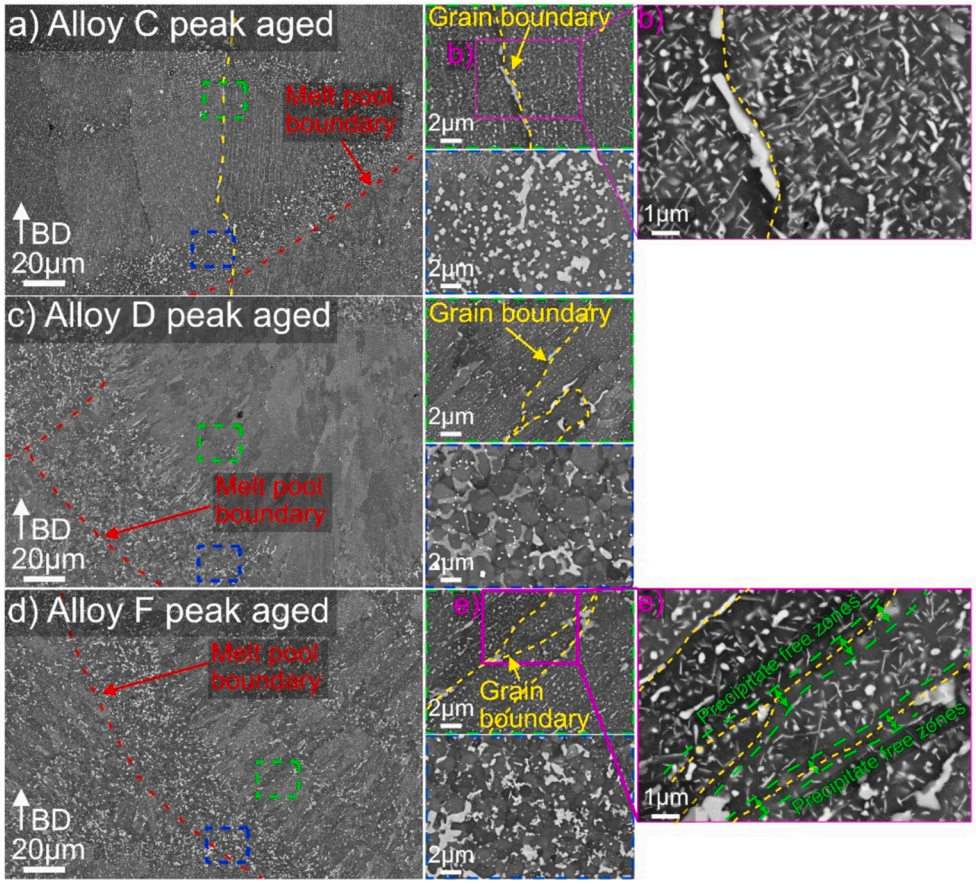

Fig. 10. Peak aged microstructure of a) Alloy C c) Alloy D and d) Alloy F along building direction (BD) at respective peak aged condition (HT2). Melt pool boundaries and grain boundaries are marked with red and yellow dotted lines respectively. The insets for each micrograph represent the high-resolution image of the interior of the melt pool (green) and melt pool boundary (blue) region. Within the grain boundary region, another inset (purple) shows the needle-/plate- shaped nano precipitates formed in b) alloy C and e) alloy F respectively. In the case of alloy F, precipitate-free zones are shown between green dotted zones around grain boundaries. (For interpretation of the references to colour in this figure legend, the reader is referred to the web version of this article.)

A well-known fact for precipitation-hardened Al-alloys is the dip in ductility observed during tensile loading post-heat treatments [28,47]. Though homogeneous precipitation of finely dispersed precipitates strengthens the material, localised inhomogeneities in the matrix lead to strain concentration formed upon heat treatments. In the materials we have studied, two such areas have been characterized in Fig. 9 and Fig. 10 namely melt pool boundaries and grain boundaries. Fig. 4 shows the fracture surfaces of some of the alloys tested at room temperature. In general, all the alloys showed the formation of micro dimples indicating ductile failure. Upon closer investigation in Alloy C and F tested along Z direction (HT2 condition), a distinct fracture along melt pool tracks rich in melt pool boundary precipitates was seen. Although these precipitates exist in as-printed conditions, we believe that the depletion of fine needle-/plate- shaped precipitates upon heat treatments in these regions (see Fig. 10a)) causes the formation of soft zones. During tensile loading beyond the yield point, such areas will act as strain concentration sites due to loss of solutes, the distance between precipitates and the size/shape of these melt pool boundary precipitates. The same is also true for alloy F and considering the increased amount of primary precipitates at melt pool boundaries, this effect is more pronounced, reducing the ductility to ~ 5 % in HT2 condition. Along XY direction (Fig. 4c)), it is seen that intergranular fracture can take place with fracture surfaces along grain boundaries. Similar to loading along the Z direction, strain concentration sites are formed around larger grain boundary precipitates (see Fig. 10a),c)). However, the width of the depleted zone is less (1–2 μm) as compared to the melt pool boundary region (10–15 μm) which could be the major reason for higher ductility along XY direction for all three alloys in HT conditions.

For high-temperature tensile testing, alloy C retains 45 % of RT strength at 573 K whereas alloy F drops to 23 % of RT strength. The main reasons, as attributed in literature [27,49,50,51,52] for the reduction in strength at high temperatures are dislocation climb and grain boundary sliding which gets activated at higher temperatures. We believe there are two reasons to alloy F loses significantly more strength. Dislocation climb relieves the pile-up of dislocations against grain boundaries, thereby significantly weakening the grain boundary effect, especially in alloy F with finer grains [52]. Additionally, the high temperatures of testing (>523 K) might start to coarsen the Mn precipitates during soaking and high-temperature testing as their volume fraction is much higher (0.14) as compared to alloy C (0.03); see supplementary section for details on data. This would lead to a loss in strength from these precipitates. One solution for optimising the properties of alloy F would be to thus underage the samples (648 K 6 h). This would slightly reduce the yield strength at room temperature, but it could in turn enhance the ductility and high-temperature performance.

Fractography was conducted to study the ductility loss of samples during high-temperature tests, see Fig. 7. Along the Z direction, a similar trend of fracture (as RT samples) along melt pool tracks was observed both for alloy C and F. Additionally, the fracture surface also progressed perpendicular to melt pool tracks, which was seen to be rich in precipitates. The orientation and size of features suggest that these resemble the distance between solidification (cell) boundaries which are rich in needle-shaped precipitates. This means additional sites for fracture were available thus affecting the ductility of the sample. Along the XY

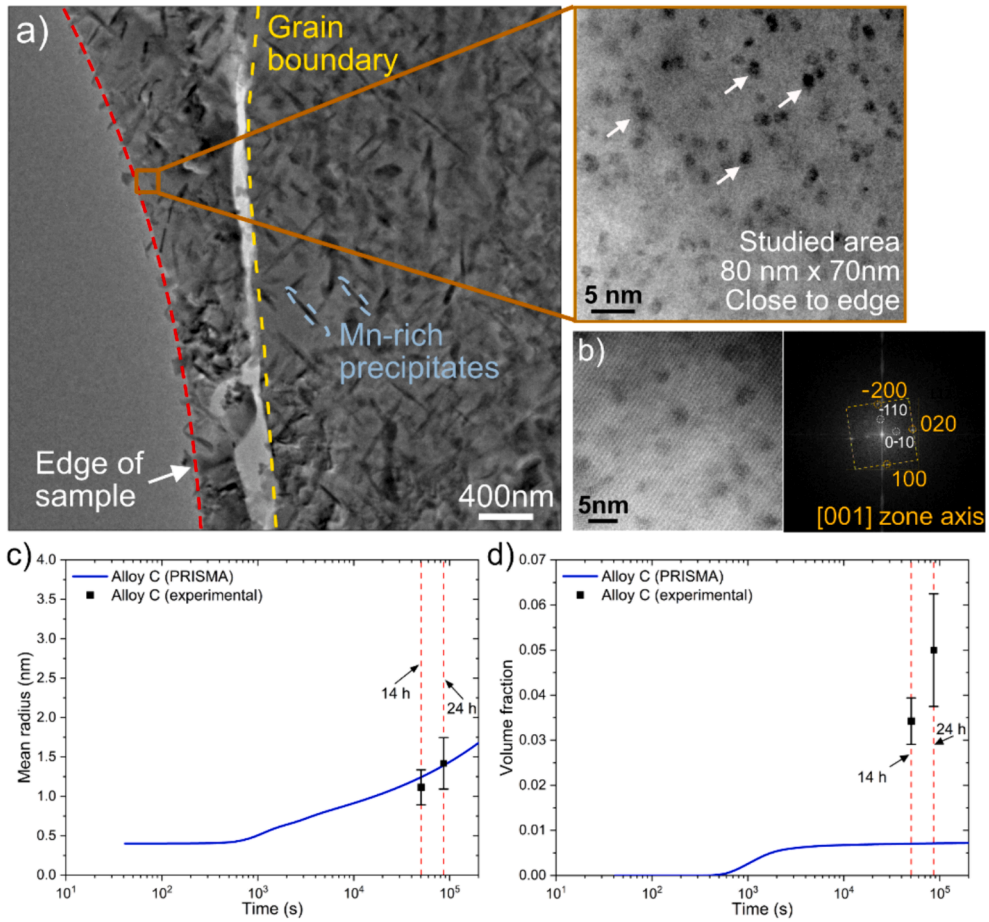

Fig. 11. TEM foil representing Alloy C HT2 sample (648 K 14 h) is shown. a) TEM image shows the section close to the edge of thinned foil (red) that was studied, close to which a grain boundary (yellow) and some Mn-rich precipitates are seen (blue). The inset (brown) shows one of the areas studied with spherical Al-Zr precipitates (white arrow) b) Fast-Fourier transform (FFT) image along [001] zone axis confirming the presence of precipitates c)-d) Evolution of mean radius (nm) and volume fraction over time with comparison of theoretical (PRISMA) results with experimental values from TEM. (For interpretation of the references to colour in this figure legend, the reader is referred to the web version of this article.)

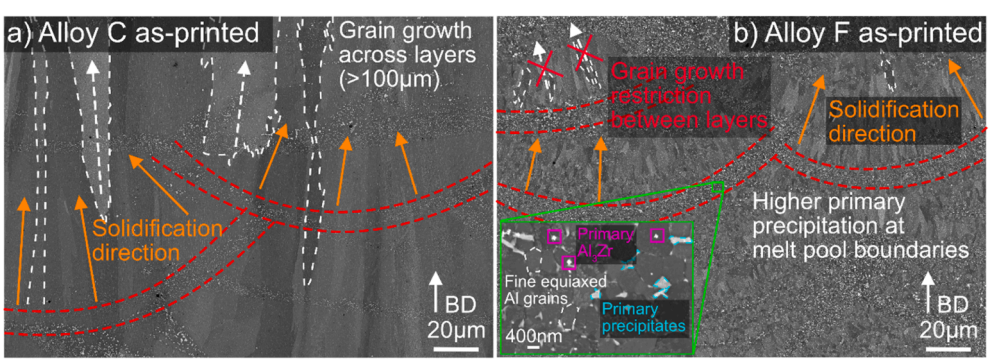

Fig. 12. Microstructural development in a) Alloy C and b) Alloy F respectively. Inset (green) shows different primary precipitates formed in alloy F. (For interpretation of the references to colour in this figure legend, the reader is referred to the web version of this article.)

direction, the ductility dip is severe (8 % →2%) and the fractography reveals that intergranular fracture is seen together with intragranular fracture along solidification boundary precipitates similar to the Z direction. The main reason is similar in that higher sites of fracture are available and when loaded along XY direction, these sites are perpendicular to loading. This means that the localised failure sites (solidification boundaries) are ~ 1–2 μm apart. The reason why alloy F has an increase in ductility is unclear, and it is not investigated further in this paper. Fig. 8 shows that at room temperature, increasing the strain rate ($0.01\ \%\ s^{-1} \rightarrow 1\ \%\ s^{-1}$) enhances the work hardening thereby increasing the UTS. A similar observation could be made comparing tensile tests in Fig. 3 and Fig. 6, with higher work hardening at lower temperatures. The high strain rate, temperature tests in Fig. 8b) show a similar increase in UTS. However, at the same time, there is a significant increase in the ductility of the material. For Al-Y-Ni-Fe alloy [53] and Al-Si alloy [54] a loss in ductility was observed at high temperatures. In the former case at higher strain rates, the ductility increased. They related it to the strong localisation of deformation in precipitation-hardened materials which

Table 3
Comparison of actual yield strength (MPa) compared to calculated sum of strengthening contributions (MPa). The solid solution effect corresponds to the remaining strength (MPa). The actual yield strengths are averaged along Z and XY directions and error intervals represent one standard deviation.

Alloy	Actual yield strength	The sum of contributions ($\sigma_0 + \Delta\sigma_{GB} + \Delta\sigma_{Dis} + \Delta\sigma_{Ppt}$)	Remaining strength (Actual yield strength – sum of contributions)
Alloy C as-printed	249 ± 0.3 MPa	112 MPa (10 + 21 + 42 + 39)	137 MPa
Alloy C peak aged	350 ± 6.9 MPa	279 MPa (10 + 21 + 6 + 242)	71 MPa
Alloy F as-printed	389 ± 16.3 MPa	215 MPa (10 + 89 + 42 + 74)	174 MPa
Alloy F peak aged	502 ± 3.9 MPa	479 MPa (10 + 89 + 6 + 374)	23 MPa

are relevant at low strain rates only.

4.3. Summary of tensile properties

Fig. 13 provides property maps for Al-Mn-Cr-Zr alloys as compared to other AM alloys or conventional cast/wrought alloys. PBF-LB techniques in as-printed conditions show low precipitation and mostly solid solution strengthening thus creating medium-strength (~250 MPa) alloys combined with high ductility (~25 %). Structural applications on the other hand require higher strength from Al-alloys. Thus, precipitation-hardened alloys are desirable with ~ 500 MPa yield strength [14,28]. The alloy systems we have proposed can reach such competitive values in yield strength thus meeting our performance criteria of > 450 MPa strength. One advantage of these alloys is that the direct ageing heat treatments do not require any solution step unlike the T6-like heat treatments [55].

4.4. Summary of high-temperature tensile properties

Al-alloys are not well known for good high-temperature properties. Most Al-Cu or Al-Zn-based high-strength alloys perform poorly at temperatures as high as 573 K retaining < 15 % RT strengths (see Fig. 14). Other attempts made in PBF-LB technique such as Al-Ce-Mn alloys [29] show excellent high-temperature properties. The limitation of these alloys was relatively poorer room temperature properties (<300 MPa yield and < 5 % ductility). Another example is Al-Fe-Cr alloy [30] which performs extremely well. The alloys presented by us have been tested to 573 K and one of the alloys (alloy C) outperforms most of the alloys at this temperature. Alloy F retains up to 110 MPa yield strength at 573 K. This shows the potential of novel Al-alloys designed to increase the maximum service temperature for Al-alloys to about 550–600 K [26,27]. The primary strength in these alloys at high temperatures is proposed to come from thermally stable nanoprecipitates. However, two limitations should be pointed out. The alloys tested in this study do not increase in ductility when the temperature of testing increases, as is usually true for Al-alloys. Additionally, the soaking time used by us was two hours at the set temperature. Other authors have either not mentioned it or used low times such as 10–30 min. The strain rates used by others are also high by 1–2 orders of magnitude, which may end up overestimating the strength (see Fig. 8). There is no exact standard testing method for AM components, as this depends on the application the material is aimed for. The closest standard we found was EN2002-002 [59] which is used by EOS for qualifying Al2139 alloy for aerospace applications. There has been different ductility reported when different soaking times were used for Al-Ce-Mn alloys [29]. However, we have already reported promising results on the high-temperature thermal stability of these alloys which should complement this work [33] and soaking time might have relatively small effects.

5. Conclusions

This study provides the reader with an extensive overview of the room temperature and high temperature uniaxial tensile properties of the Al-Mn-Cr-Zr based alloy system produced with PBF-LB. In as-printed conditions, high supersaturation of solutes gives a ductile behaviour of test bars (~25 %). Via direct ageing heat treatments, the alloys gain significant strength via precipitation hardening reaching up to 500 MPa yield strength. At high temperatures, yield strength up to 170 MPa at 573 K is observed. Most of the strength comes from Al_3Zr nanoprecipitates which are ~ 1 nm in peak aged condition as characterised with high resolution microscopy. The overall properties of the alloys are repeatable and on par with other commercial Al-alloys for high temperature use produced conventionally or via AM. These properties thus showcase high-temperature alloys which can increase operating temperatures for Al-alloys up to 550 K – 600 K by doubling the strength against conventional Al-alloys.

CRediT authorship contribution statement

Bharat Mehta: Writing – original draft, Visualization, Validation, Software, Project administration, Methodology, Investigation, Formal analysis, Data curation, Conceptualization. **Sven Bengtsson:** Writing – review & editing, Validation, Supervision, Resources, Methodology, Investigation, Formal analysis, Conceptualization. **Dmitri Riabov:** Writing – review & editing, Visualization, Validation, Methodology,

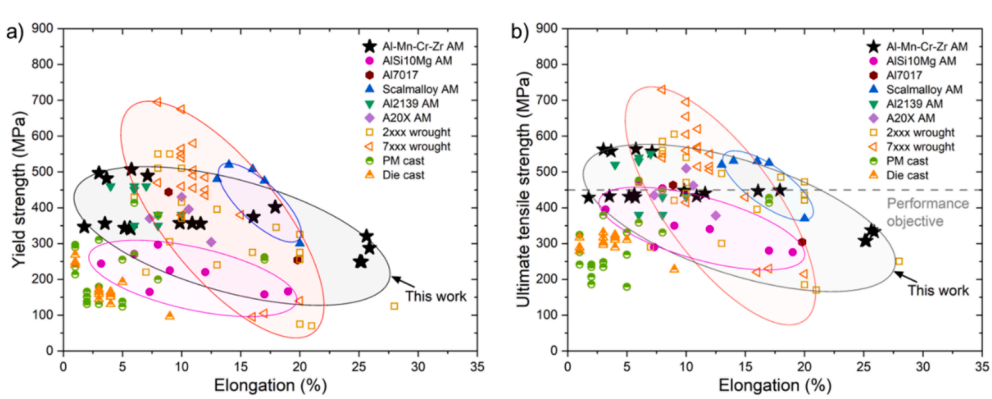

Fig. 13. Summary of elongation (%) on X-axis and a) yield strength (MPa) and b) ultimate tensile strength (MPa) for various AM (PBF-LB only), wrought and cast Al-alloys. For AM alloys, the values for AlSi10Mg taken from [56,57,58], Scalmalloy® [15,16,36,56], Al2139 [19] and A20X® [17,18]. Wrought alloy values were taken from [28] and cast alloys from [13]. For this work, one representative value for each of the 18 conditions was taken as a data point.

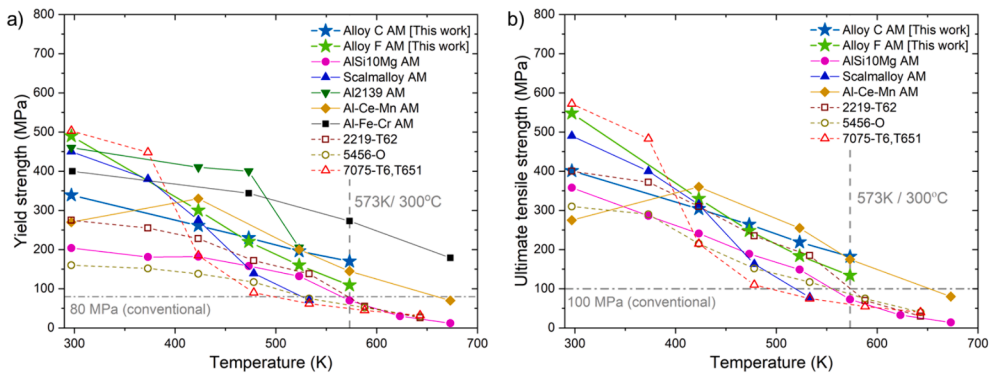

Fig. 14. Summary of high-temperature strength (MPa) at various temperatures (up to 673 K) for various AM (PBF-LB only) and wrought Al-alloys. The values for AlSi10Mg were taken from [60], Scalmalloy® and Al-Ce-Mn from [29], Al2139 from [19] and Al-Fe-Cr from [30]. Wrought alloy values are taken from [14].

Investigation, Formal analysis, Data curation. **Elanghovan Natesan:** Writing – review & editing, Validation, Methodology, Investigation, Formal analysis. **Karin Frisk:** Writing – review & editing, Validation, Supervision, Methodology, Data curation, Conceptualization. **Johan Ahlström:** Writing – review & editing, Visualization, Supervision, Data curation, Conceptualization. **Lars Nyborg:** Writing – review & editing, Visualization, Validation, Supervision, Funding acquisition.

Declaration of competing interest

The authors declare that they have no known competing financial interests or personal relationships that could have appeared to influence the work reported in this paper.

Data availability

The raw/processed data required to reproduce these findings cannot be shared at this time due to technical or time limitations. It can be made available later upon reasonable request.

Acknowledgements

The authors would like to acknowledge funding from European Union's Horizon 2020 Research and Innovation Programme, Sweden under grant agreement 820774, through project MANUELA- Additive Manufacturing using Metal Pilot Line. This work is also funded by Centre of Additive Manufacturing- Metal (CAM2) hosted by Chalmers University of Technology which is sponsored via VINNOVA grant number 2016–05175. Authors would also like to acknowledge support from Production Area of Advance at Chalmers University, FORMAS and Energimyndigheten. Dr. Andreas Markström is acknowledged for providing the latest version of TCAL, MOBAL databases and Thermo-Calc software

Appendix A. Supplementary data

Supplementary data to this article can be found online at https://doi.org/10.1016/j.matdes.2024.113160.

References

[1] D.D. Gu, W. Meiners, K. Wissenbach, R. Poprawe, Laser additive manufacturing of metallic components: Materials, processes and mechanisms, Int. Mater. Rev. 57 (3) (2012) 133–164, https://doi.org/10.1179/1743280411Y.0000000014.
[2] B. Blakey-Milner, et al., Metal additive manufacturing in aerospace: A review, Mater Des 209 (2021) 110008, https://doi.org/10.1016/j.matdes.2021.110008.
[3] "Wohlers Report 2022," 2022.
[4] C. Emmelmann, P. Sander, J. Kranz, E. Wycisk, Laser additive manufacturing and bionics: Redefining lightweight design, in: Physics Procedia, Elsevier B.V, 2011, pp. 364–368, https://doi.org/10.1016/j.phpro.2011.03.046.
[5] C. Yan, L. Hao, A. Hussein, S.L. Bubb, P. Young, D. Raymont, Evaluation of light-weight AlSi10Mg periodic cellular lattice structures fabricated via direct metal laser sintering, J Mater Process Technol 214 (4) (2014) 856–864, https://doi.org/10.1016/j.jmatprotec.2013.12.004.
[6] N. T. Aboulkhair, M. Simonelli, L. Parry, I. Ashcroft, C. Tuck, and R. Hague, "3D printing of Aluminium alloys: Additive Manufacturing of Aluminium alloys using selective laser melting," *Prog Mater Sci*, vol. 106, no. August 2018, p. 100578, 2019, doi: 10.1016/j.pmatsci.2019.100578.
[7] T. Han, et al., Effect of cooling rate on microstructure and mechanical properties of AlCrFe2Ni2 medium entropy alloy fabricated by laser powder bed fusion, J. Mater. Res. Technol. 25 (2023) 4063–4073, https://doi.org/10.1016/j.jmrt.2023.06.241.
[8] H.L. Wei, et al., Mechanistic models for additive manufacturing of metallic components, Prog Mater Sci 116 (July) (2019) 2021, https://doi.org/10.1016/j.pmatsci.2020.100703.
[9] R.S. Mishra, S. Thapliyal, Design approaches for printability-performance synergy in Al alloys for laser-powder bed additive manufacturing, Mater Des 204 (2021) 109640, https://doi.org/10.1016/j.matdes.2021.109640.
[10] P.A. Rometsch, Y. Zhu, X. Wu, A. Huang, Review of high-strength aluminium alloys for additive manufacturing by laser powder bed fusion, Mater Des 219 (2022) 110779, https://doi.org/10.1016/j.matdes.2022.110779.
[11] L. Thijs, K. Kempen, J.P. Kruth, J. Van Humbeeck, Fine-structured aluminium products with controllable texture by selective laser melting of pre-alloyed AlSi10Mg powder, Acta Mater 61 (5) (2013) 1809–1819, https://doi.org/10.1016/j.actamat.2012.11.052.
[12] EOS GmbH, "EOS Aluminium AlSi10Mg Material Data Sheet EOS Aluminium AlSi10Mg Good Strength & Dynamic Load Bearing Capacity," 2022.
[13] J.G. Kaufman, Properties and Selection of Cast Aluminum Alloys, Properties and Selection of Aluminum Alloys vol. 2, no. Ref 2 (2019) 465–506, https://doi.org/10.31399/asm.hb.v02b.a0006548.
[14] ASM International, Introduction to Aluminum and Aluminum Alloys, Metals Handbook Desk Edition (1998) 417–423. doi: https://doi.org/10.31399/asm.hb.v02.9781627081627.
[15] K. Schmidtke, F. Palm, A. Hawkins, C. Emmelmann, Process and mechanical properties: Applicability of a scandium modified Al-alloy for laser additive manufacturing, Phys Procedia vol. 12, no. PART 1 (2011) 369–374, https://doi.org/10.1016/j.phpro.2011.03.047.
[16] citim, "Data Sheet Scalmalloy RP AlMgSc," Barleben. [Online]. Available: http://www.papersearch.net/view/detail.asp?detail_key=10000715.
[17] D. Sheet, "Aluminium A20X ™ Aluminium A20X ™," pp. 2–3.
[18] J. Barode, et al., Revisiting Heat Treatments for Additive Manufactured Parts: A Case Study of A20x Alloy, Mater Des 225 (2023), https://doi.org/10.2139/ssrn.4219651.
[19] EOS GmbH - Electro Optical Systems, "EOS Aluminium Al2139 AM Material Data Sheet", [Online]. Available: https://www.eos.info/03_system-related-assets/material-related-contents/metal-materials-and-examples/metal-material-datasheet/aluminium/material_datasheet_eos_aluminium_al2139-am_02-23_en.pdf.
[20] H. Jones, "Chapter 3 Rapid solidification," *Pergamon Materials Series*, vol. 2, no. C, pp. 23–45, 1999, doi: 10.1016/S1470-1804(99)80049-2.
[21] B. Mehta, L. Nyborg, K. Frisk, and E. Hryha, "Al–Mn–Cr–Zr-based alloys tailored for powder bed fusion-laser beam process: Alloy design, printability, resulting microstructure and alloy properties," *J Mater Res*, vol. 3, pp. 1–13, 2022, doi: 10.1557/s43578-022-00533-1.
[22] M. Buttard, et al., Multi-scale microstuctural investigation of a new Al-Mn-Ni-Cu-Zr aluminium alloy processed by laser powder bed fusion, Materialia (oxf) vol. 18, no. July (2021) 101160, https://doi.org/10.1016/j.mtla.2021.101160.
[23] S. Thapliyal *et al.*, "An integrated computational materials engineering-anchored closed-loop method for design of aluminum alloys for additive manufacturing," *Materialia (Oxf)*, vol. 9, no. December 2019, p. 100574, 2020, doi: 10.1016/j.mtla.2019.100574.
[24] A. Dreano, J. Favre, C. Desrayaud, P. Chanin-Lambert, A. Wimmer, M.F. Zaeh, Computational design of a crack-free aluminum alloy for additive manufacturing, Addit Manuf 55 (Jul. 2022), https://doi.org/10.1016/j.addma.2022.102876.

[25] M. Roscher, S. Balachandran, D. Mayweg, E. Jägle, Development of Al-Ti-based alloys for laser powder bed fusion, Addit Manuf 47 (June) (2021), https://doi.org/10.1016/j.addma.2021.102315.
[26] J. L. Cann *et al.*, "Sustainability through alloy design: Challenges and opportunities," *Prog Mater Sci*, vol. 117, no. July 2020, p. 100722, 2021, doi: 10.1016/j.pmatsci.2020.100722.
[27] R.A. Michi, A. Plotkowski, A. Shyam, R.R. Dehoff, S.S. Babu, Towards high-temperature applications of aluminium alloys enabled by additive manufacturing, Int. Mater. Rev. (2021), https://doi.org/10.1080/09506608.2021.1951580.
[28] J.G. Kaufman, Properties and Applications of Wrought Aluminum Alloys, Properties and Selection of Aluminum Alloys vol. 2, no. Table 2 (2019) 202–275, https://doi.org/10.31399/asm.hb.v02b.a0006543.
[29] A. Plotkowski, et al., Microstructure and properties of a high temperature Al–Ce–Mn alloy produced by additive manufacturing, Acta Mater 196 (2020) 595–608, https://doi.org/10.1016/j.actamat.2020.07.014.
[30] M. T. Perez-Prado, A. Martin, D. F. Shi, and S. Milenkovic, "An Al-5Fe-6Cr alloy with outstanding high temperature mechanical behavior by laser powder bed fusion," vol. 55, no. January, 2022, doi: 10.1016/j.addma.2022.102828.
[31] B. Mehta, K. Frisk, and L. Nyborg, "Effect of Precipitation Kinetics on Microstructure and Properties of Novel Al-Mn-Cr-Zr Based Alloys Developed for Powder Bed Fusion – Laser Beam Process," *J Alloys Compd*, 2022, [Online]. Available: https://doi.org/10.1016/j.jallcom.2022.165870.
[32] B. Mehta, K. Frisk, and L. Nyborg, "Advancing Novel Al-Mn-Cr-Zr Based Family of Alloys Tailored for Powder Bed Fusion-Laser Beam Process," *J Alloys Compd*, vol. 967, p. 171685, Aug. 2023, doi: 10.1016/j.jallcom.2023.171685.
[33] B. Mehta, K. Frisk, L. Nyborg, S. Bengtsson, and E. Hryha, "Thermal Stability In Al-Mn-Cr-Zr Based Aluminium Alloys Tailored For Powder Bed Fusion – Laser Beam," *WorldPM 2022 Congress & Exhibition : Conference Proceedings*, 2022.
[34] Thermo-Calc, "Precipitation Module (TC-PRISMA) User Guide," pp. 1–158, 2020, [Online]. Available: www.thermocalc.com.
[35] Astm, E8, "ASTM E8/E8M Standard Test Methods for Tension Testing of Metallic Materials 1", *Annual Book of ASTM Standards 4* no. C (2010) 1–27, https://doi.org/10.1520/E0008.
[36] A.B. Spierings, K. Dawson, K. Kern, F. Palm, K. Wegener, SLM-processed Sc- and Zr-modified Al-Mg alloy: Mechanical properties and microstructural effects of heat treatment, Mater. Sci. Eng. A 701 (June) (2017) 264–273, https://doi.org/10.1016/j.msea.2017.06.089.
[37] W.A. Curtin, D.L. Olmsted, L.G. Hector, A predictive mechanism for dynamic strain ageing in aluminium-magnesium alloys, Nat Mater 5 (11) (2006) 875–880, https://doi.org/10.1038/nmat1765.
[38] S. Bengtsson, B. Mehta, K. Frisk, and L. Nyborg, "New Aluminium Alloy Tailored For Powder Bed Fusion – Laser Beam Process," *WorldPM 2022 Congress & Exhibition : Conference Proceedings*, 2022.
[39] A. Martucci, B. Mehta, M. Lombardi, and L. Nyborg, "The Influence of Processing Parameters on the Al-Mn Enriched Nano-Precipitates Formation in a Novel Al-Mn-Cr-Zr Alloy Tailored for Power Bed Fusion-Laser Beam Process," *Metals (Basel)*, vol. 12, no. 8, 2022, doi: 10.3390/met12081387.
[40] I. Lazar *et al.*, "In situ Imaging of Precipitate Formation in Additively Manufactured Al-Alloys by Scanning X-ray Fluorescence." 2023. doi: https://doi.org/10.48550/arXiv.2311.14529.
[41] K.E. Knipling, D.C. Dunand, D.N. Seidman, Criteria for developing castable, creep-resistant aluminum-based alloys - A review, Int. J. Mater. Res. 97 (3) (2006) 246–265.
[42] J.R. Croteau, et al., Microstructure and mechanical properties of Al-Mg-Zr alloys processed by selective laser melting, Acta Mater 153 (Jul. 2018) 35–44, https://doi.org/10.1016/j.actamat.2018.04.053.
[43] G. Bergerhoff, I.D. Brown, F. Allen, Crystallographic databases, International Union of Crystallography 360 (1987) 77–95.
[44] A. Leicht, *Laser powder bed fusion of 316L stainless steel Microstructure and mechanical properties as a function of process*. 2020.
[45] T. DebRoy, et al., Additive manufacturing of metallic components – Process, structure and properties, Prog Mater Sci 92 (2018) 112–224, https://doi.org/10.1016/j.pmatsci.2017.10.001.
[46] S. Griffiths, M.D. Rossell, J. Croteau, N.Q. Vo, D.C. Dunand, C. Leinenbach, Effect of laser rescanning on the grain microstructure of a selective laser melted Al-Mg-Zr alloy, Mater Charact 143 (November) (2018), https://doi.org/10.1016/j.matchar.2018.03.033.
[47] D. S. Mackenzie and H. International, "Metallurgy of Heat Treatable Aluminum Alloys," vol. 4, 2016, doi: 10.31399/asm.hb.v04e.a0006287.
[48] M. Roscher, "Development of high-strength Aluminum alloys for Laser Powder Bed Fusion," 2022.
[49] T. Watanabe, Grain boundary design and control for high temperature materials, Mater. Sci. Eng. A 166 (1–2) (1993) 11–28, https://doi.org/10.1016/0921-5093(93)90306-Y.
[50] M.R. Drury, F.J. Humphreys, The development of microstructure in Al-5% Mg during high temperature deformation, Acta Metall. 34 (11) (1986) 2259–2271, https://doi.org/10.1016/0001-6160(86)90171-9.
[51] S. Griffiths, et al., Coarsening- and creep resistance of precipitation-strengthened Al–Mg–Zr alloys processed by selective laser melting, Acta Mater 188 (2020) 192–202, https://doi.org/10.1016/j.actamat.2020.02.008.
[52] M. Huang, Z. Li, J. Tong, The influence of dislocation climb on the mechanical behavior of polycrystals and grain size effect at elevated temperature, Int J Plast 61 (2014) 112–127, https://doi.org/10.1016/j.ijplas.2014.06.002.
[53] X.L. Shi, R.S. Mishra, T.J. Watson, Effect of temperature and strain rate on tensile behavior of ultrafine-grained aluminum alloys, Mater. Sci. Eng. A 494 (1–2) (2008) 247–252, https://doi.org/10.1016/j.msea.2008.06.044.
[54] G. Rajaram, S. Kumaran, T.S. Rao, High temperature tensile and wear behaviour of aluminum silicon alloy, Mater. Sci. Eng. A 528 (1) (2010) 247–253, https://doi.org/10.1016/j.msea.2010.09.020.
[55] T.H.E. Major, A. Alloy, Heat Treatment Practices of Age-Hardenable Aluminum Alloys *, c 4 (2016) no, https://doi.org/10.31399/asm.hb.v04e.a0006288.
[56] P.D. Nezhadfar, S. Thompson, A. Saharan, N. Phan, N. Shamsaei, Structural integrity of additively manufactured aluminum alloys : Effects of build orientation on microstructure, porosity, and fatigue behavior, Addit Manuf vol. 47, no. August (2021) 102292, https://doi.org/10.1016/j.addma.2021.102292.
[57] EOS GmbH - Electro Optical Systems, "Material Data Sheet: EOS Aluminium AlSi10Mg," vol. 49, no. 0, pp. 1–5, 2014, [Online]. Available: http://gpiprototype.com/images/PDF/EOS_Aluminium_AlSi10Mg_en.pdf.
[58] "AlSi10Mg material datasheet: SLM Solutions." Accessed: Aug. 05, 2022. [Online]. Available: https://www.slm-solutions.com/fileadmin/Content/Powder/MDS/MDS_Al-Alloy_AlSi10Mg_0520_EN.pdf.
[59] C. S. I. S. Reproduction, "EN2002 002 Aerospace series – Metallic materials – Test methods – Part 2 : Tensile testing at elevated temperature," 2022.
[60] N.E. Uzan, R. Shneck, O. Yeheskel, N. Frage, High-temperature mechanical properties of AlSi10Mg specimens fabricated by additive manufacturing using selective laser melting technologies (AM-SLM), Addit Manuf 24 (October) (2018) 257–263, https://doi.org/10.1016/j.addma.2018.09.033.